Modeling soot formation in premixed flames using an Extended Conditional Quadrature Method of Moments

Steffen Salenbauch [a,*], Alberto Cuoci [b], Alessio Frassoldati [b], Chiara Saggese [b], Tiziano Faravelli [b], Christian Hasse [a]

[a] *Chair of Numerical Thermo-Fluid Dynamics, Department of Energy Process Engineering and Chemical Engineering, TU Bergakademie Freiberg, Fuchsmühlenweg 9, Freiberg 09599, Germany*
[b] *Department of Chemistry, Materials and Chemical Engineering, Politecnico di Milano, Piazza Leonardo da Vinci 32, 20133 Milano, Italy*

Received 17 November 2014
Received in revised form 5 March 2015
Accepted 6 March 2015
Available online 26 March 2015

1. Introduction

Soot particle formation in combustion has an impact on both combustion efficiency and human health. In terms of legislation, the limitations on soot emissions are tending to become even stricter regarding both volume and number density. In addition, soot plays an important role in radiative heat transfer, where accurate but efficient prediction of the soot evolution is required to precisely model the radiative fluxes in systems like fires [3,4].

Nowadays, most of the detailed phenomenological soot models are based on techniques for solving the population balance equation (PBE), which is a continuity statement written in terms of a number density function (NDF) [5].

Among them, Monte Carlo (MC) based models were developed in order to approximate the PBE-governed soot particle population using an ensemble of stochastic particles [6–12]. Monte Carlo methods are known to yield very accurate results; however, due to their computational expense, their applicability has so far been limited to simple configurations.

Another group of approaches, referred to as Sectional Methods, are based on the separation of the particle size spectrum into a set of size classes [13–22]. While these methods are easy to implement and give detailed information on the particle size distribution, sectional methods are also numerically expensive, especially if the shape of soot particles is described by more than one size property.

The computationally most efficient approach to solving the PBE is given by moment methods. Here, the NDF is not solved directly; instead only a few lower-order moments of the distribution are tracked. As discussed later, this transformation yields unclosed

* Corresponding author. Fax: +49 3731 394555.
E-mail address: Steffen.Salenbauch@iec.tu-freiberg.de (S. Salenbauch).

terms in the moment equations. The most widely used moment closure approach is given by the Method of Moments with Interpolative Closure (MOMIC), where unknown moments are interpolated from known ones [23–34].

Another way to achieve closure is given by the Quadrature Method of Moments (QMOM), where the unknown NDF is approximated either by a set of Dirac delta functions or, in newer developments, by kernel density functions [1]. Within recent years, QMOM-based soot models have been applied increasingly [35–40]. Beside univariate approaches, which assume soot particles to be spherical, quasi-multivariate and multivariate approaches have also been developed. Multivariate models offer the possibility to consider aggregation and therefore lead to a more realistic description of the shape of soot particles. However, the univariate moment inversion concept is not easily transferable to multivariate cases [41–43]. Therefore, multivariate moment problems are usually treated using the *Direct Quadrature Method of Moments* (DQMOM) [44]. For instance, Blanquart and Pitsch [39] developed a detailed, trivariate DQMOM-based soot model. The comparison of the results with MC simulations showed that DQMOM yields very accurate results for the PBE. However, DQMOM approaches are numerically challenging, since they require the inversion of a linear system, which may be extremely ill-conditioned [5,45]. Mueller et al. [45,46] therefore suggested a new bivariate approach called *Hybrid Method of Moments* (HMOM), in order to combine the numerical stability of MOMIC with the accuracy of the DQMOM method. The comparison between HMOM, DQMOM and a bivariate MOMIC approach with a MC simulation revealed that the evolution of the soot mass is described adequately using all the moment methods tested [34]. However, with the exception of DQMOM, the moment methods yield deviations from the MC simulations regarding the temporal evolution of the particle number density.

Besides numerical stability and accuracy issues, one of the most severe restrictions of state-of-the-art moment methods is the lack of a resolved NDF. Due to this, source terms in the transport equations cannot be formulated as a continuous function of the particle size. Thus, effects such as the reduced collision efficiency of the smallest particles [47,48] cannot be implemented accurately in standard moment methods with the same precision as in MC.

In order to overcome these limitations, Yuan et al. [1] proposed an *Extended Quadrature Method of Moments* (EQMOM), which enables the shape of the particle size distribution to be reconstructed from a moment set using kernel density functions instead of Dirac delta functions. EQMOM was evaluated for 13 benchmark test cases and further applied to model radiation transport [49], but not yet to model soot formation in flames.

However, EQMOM is a univariate moment method and, therefore, the aggregation of soot particles cannot be accounted for accurately. It is known that even small particles can build aggregates upon collision [33,50–52]. Therefore, aggregation needs to be considered in soot models in order to describe the evolution of soot particle ensembles properly. This implies the application of a bivariate NDF. Yuan and Fox [2] developed a multivariate moment approach called *Conditional Quadrature Method of Moments* (CQMOM) to handle bivariate moment formulations in a numerically robust way. The suitability of CQMOM to describe particle ensembles has already been demonstrated by modeling TiO_2 formation in flames [53,54]. However, in contrast to EQMOM, CQMOM is based on the standard Gaussian-QMOM tech-nique and the NDF is thus not known. A possible modification to standard QMOM techniques such as CQMOM is given by QMOM-Radau, where the Gauss-Radau quadrature interpolation rule is applied to fix a quadrature node at the smallest particle size [55]. However, to the authors' knowledge, QMOM-Radau based approaches have not yet been published for particles or even soot so far.

The scope of this paper is to apply EQMOM and CQMOM to model soot formation in premixed flames. The two models are ini-tially used separately. Then, a combination of the two models, called the *Extended Conditional Quadrature Method of Moments* (ECQMOM) [5], is formulated for sooting flames. To do so, the pro-cesses of nucleation, coagulation, condensation and HACA surface growth [12,25,29] are formulated in the context of an EQMOM and a CQMOM approach. In order to obtain a numerically stable moment method, which resolves the soot particle size distribution and captures aggregation, the two approaches are combined to form the ECQMOM method. Special focus is put on the methods' capability to close the moment source terms accurately by compar-ing the EQMOM-based methods to Gaussian-QMOM models and a MC approach [56]. The gas phase is modeled using a modified ver-sion of the extensively validated CRECK mechanism [57–61]. In order to be consistent with the soot model, pyrene (A4-$C_{16}H_{10}$) is set as the largest polycyclic aromatic hydrocarbon (PAH) species in the model, which accounts for all larger ones.

The remainder of this paper is organized as follows: First, the numerical model is introduced and explained in Section 2. The methods of EQMOM, QMOM-Radau, CQMOM and ECQMOM are used to model soot for the first time. Therefore, detailed explana-tions are given on the application of these methods to the soot model. Next, the kinetic scheme to describe the gas phase is explained. Afterwards, the ability of this scheme to predict with accuracy not only the major species of a fuel-rich flame, but also PAH species is demonstrated in Section 3, where the model is com-pared to experimental results [62–68]. The kinetic mechanism is then applied to model the gas phase of two sooting reference flames, which serve as validation cases for the moment-based soot models. This involves the simulation results with the univariate EQMOM method being compared to experiments as well as to QMOM, QMOM-Radau and MC results for a premixed burner-stabi-lized ethylene flame, where aggregation was found to be negligible [69]. A similar comparison to experiments, CQMOM and MC sim-ulations follows for the bivariate ECQMOM soot model introduced. Here, another burner-stabilized ethylene flame, where aggregation is known to be an important effect [70], is chosen as the test flame. Finally, conclusions are drawn in Section 4.

2. Numerical model

2.1. Method of moments

The evolution of the soot NDF $n(t, \mathbf{x}; \xi)$ in fuel-rich premixed flames is governed by the PBE:

$$\frac{\partial n(t,\mathbf{x};\xi)}{\partial t} + \frac{\partial \mathbf{u} n(t,\mathbf{x};\xi)}{\partial \mathbf{x}} = \dot{n}(t,\mathbf{x};\xi). \quad (1)$$

In this study, diffusive terms are neglected. For molecular diffusion, this is justified by the high Schmidt number of soot particles, as shown by Bisetti et al. [71]. In addition, thermophoresis is known to have only a minor effect on the transport velocity of soot parti-cles in premixed flames [70,72,73]. Therefore, in this study, soot particles move along the axis with the local gas velocity. The source term $\dot{n}(t, \mathbf{x}, \xi)$ accounts for the physical and chemical processes of particle nucleation $\dot{n}_{nuc}$, coagulation $\dot{n}_{coag}$, PAH condensation $\dot{n}_{cond}$ and chemical surface growth $\dot{n}_{sg}$:

$$\dot{n}(t,\mathbf{x};\xi) = \dot{n}_{nuc}(t,\mathbf{x}) + \dot{n}_{coag}(t,\mathbf{x};\xi) + \dot{n}_{cond}(t,\mathbf{x};\xi) + \dot{n}_{sg}(t,\mathbf{x};\xi). \quad (2)$$

In this study, we put the focus on fuel-rich premixed flames. Therefore, soot particle oxidation is not considered, as previous studies have shown that oxidation has a minor effect on the soot evolution in fuel-rich premixed flames [6,24,70,74]. This is confirmed by Xu et al. [70], who experimentally and numerically

investigated one of the test flames considered in this paper below (cf. Section 2.4).

The vector of the internal coordinates ξ contains the properties to characterize the soot particles. In the first part of this work, soot particles are characterized univariately by considering their volume V

$$\xi = (V). \tag{3}$$

However, in order to describe the shape of soot particles in a more realistic way, a bivariate description is needed. Therefore, ξ needs to be extended to both the particle volume V and the particle surface S

$$\xi = (V,S)^T. \tag{4}$$

The bivariate description allows aggregation effects to be modeled, whereas for the univariate model all particles are assumed to be spherical.

Since the PBE is high-dimensional, a direct solution is not feasible for soot ensembles. In moment methods, the PBE is transformed to moment equations using the definition of the k-th moment of the univariate NDF

$$m_k(t,\mathbf{x}) = \int_0^\infty V^k n(t,\mathbf{x};V)dV. \tag{5}$$

Keeping in mind that the lower bound of the particle size spectrum is given by the volume of a freshly nucleated particle denoted as V_1, Eq. (5) is equivalent to

$$m_k(t,\mathbf{x}) = \int_{V_1}^\infty V^k n(t,\mathbf{x};V)dV, \tag{6}$$

and this is further discussed below. For the bivariate NDF, the k,l-th moment is defined as

$$m_{k,l}(t,\mathbf{x}) = \int_0^\infty \int_0^\infty V^k S^l n(t,\mathbf{x};V,S)dSdV. \tag{7}$$

It should be noted, that time and space dependencies are dropped in the remainder of this paper for brevity. Eqs. (5) and (7) lead to transport equations for the moments (presented here for the univariate case):

$$\frac{\partial m_k}{\partial t} + \frac{\partial \mathbf{u} m_k}{\partial \mathbf{x}} = \dot{m}_k. \tag{8}$$

For numerical reasons, Eq. (8) is transformed into a system of ordinary differential equations with the time being the only independent coordinate, following the idea of Blanquart [75].

In the remainder of the paper, we focus on the coagulation source term. Thus, again considering only the univariate case for brevity, the moment transformation for $\dot{m}_{k,coag}$ yields [1]

$$\dot{m}_{k,coag} = \int_0^\infty V^k \left[\frac{1}{2}\int_0^V \beta(V-V',V')n(V-V')n(V')dV' - \int_0^\infty \beta(V,V')n(V)n(V')dV'\right]dV. \tag{9}$$

As the coagulation kernel $\beta(V)$ for the free molecular and continuum regime depends on V, the RHS of Eq. (9) is unclosed. Closure can be achieved using the quadrature-based moment methods described next.

First, a short review of the standard QMOM theory is provided to create a basis for demonstrating the characteristic properties of the enhanced QMOM-based methods. Afterwards, the QMOM-Radau extension is presented, which enables us to consider the smallest soot particles within the standard QMOM framework. A NDF reconstruction can be achieved by the EQMOM model, which is explained afterwards. Finally, the bivariate models CQMOM and ECQMOM are introduced; these are needed to extend the univariate models, taking into account particle aggregation.

2.1.1. QMOM

Since standard QMOM is a univariate model, the following equations are presented for $\xi = (V)$. The general idea behind QMOM is to approximate the unknown NDF by a linear combination of N_V Dirac delta functions

$$n(V) \approx \sum_{\alpha=1}^{N_V} w_\alpha \delta(V - V_\alpha). \tag{10}$$

Applying the moment definition of Eq. (5) to Eq. (10) leads to

$$m_k = \int_0^\infty V^k n(V)dV = \sum_{\alpha=1}^{N_V} w_\alpha V_\alpha^k. \tag{11}$$

The source terms of Eq. (2) are closed according to

$$\int_0^\infty f(V)n(V)dV \approx \sum_{\alpha=1}^{N_V} w_\alpha f(V_\alpha), \tag{12}$$

where $f(V)$ contains all parts of the source terms except the NDF itself [5], V_α and w_α are the N_V nodes and weights of the quadrature interpolation formula. As an example, the coagulation source term (see Eq. (9)) can be written as a function of the quadrature nodes and weights [1]:

$$\dot{m}_{k,coag} = \frac{1}{2}\sum_{i=1}^{N_V}\sum_{j=1}^{N_V} w_i w_j \beta(V_i,V_j)\left[(V_i+V_j)^k - V_i^k - V_j^k\right]. \tag{13}$$

The nodes and weights are computed from the known lower-order moments, solving a nonlinear system of equations:

$$\begin{aligned} m_0 &= \sum_{\alpha=1}^{N_V} w_\alpha, \\ m_1 &= \sum_{\alpha=1}^{N_V} w_\alpha V_\alpha, \\ &\vdots \\ m_{2N_V-1} &= \sum_{\alpha=1}^{N_V} w_\alpha V_\alpha^{2N_V-1}. \end{aligned} \tag{14}$$

The direct solution of this system is not feasible [5]. Instead, the relationship between the NDF and polynomials which are orthogonal to the NDF can be used. These orthogonal polynomials P_γ can be written in terms of a recursive formula

$$P_{\gamma+1}(V) = (V - a_\gamma)P_\gamma(V) - b_\gamma P_{\gamma-1}(V), \quad \gamma \in \mathbb{N}, \tag{15}$$

and can be evaluated, once the recursive coefficients a_γ and b_γ are known. In QMOM, these coefficients are given by the known lower-order moments of the soot NDF:

$$\begin{aligned} a_0 &= \frac{m_1}{m_0}, \\ a_1 &= \frac{m_3 m_0^2 + m_1^3 - 2m_2 m_1 m_0}{m_2 m_0 + m_1^2 - 2m_1^2 m_0}, \\ b_1 &= \frac{m_2 m_0 + m_1^2 - 2m_1^2 m_0}{m_0^2}, \\ &\vdots \end{aligned} \tag{16}$$

The recursion coefficients are used to fill a tridiagonal symmetric Jacobi matrix

$$\mathbf{J} = \begin{vmatrix} a_0 & \sqrt{b_1} & & & \\ \sqrt{b_1} & a_1 & \sqrt{b_2} & & \\ & \sqrt{b_2} & \ddots & \ddots & \\ & & \ddots & \ddots & \sqrt{b_{N_V-1}} \\ & & & \sqrt{b_{N_V-1}} & a_{N_V-1} \end{vmatrix}, \tag{17}$$

where the eigenvalues directly represent the nodes V_α. The eigenvectors can be used to calculate the weights w_α. We will come back to the determination of the recursive coefficients in the context of EQMOM.

In order to realize the moment inversion step presented in an efficient way, special algorithms like the product-difference algorithm [76] or the Wheeler algorithm [77] are available in the literature [5]. In this study the Wheeler algorithm is applied.

For further details on the corresponding mathematical theory, the reader is referred to [5,55,76,77].

2.1.2. Gauss-Radau QMOM

In standard QMOM, the positions of the N_V nodes are not prescribed, but they are chosen to optimize the precision of the interpolation formula Eq. (12) to a maximum degree of $2N_V - 1$. In Gauss-Radau quadrature, the position of one node is prescribed a priori (fixed) and the additional nodes and all weights are optimized to reach a degree of exactness of $2N_V - 2$. The prescribed node is fixed at the lower or upper end of the integration interval. In this study, the method is used to fix an interpolation node at the position of the particles with the smallest volume V_1. As will be shown later in the results, this concept can be used to improve the ability of the standard QMOM method, to improve the statistical representation of the smallest soot particles. In contrast to Eq. (12), the interpolation equation for Gauss-Radau QMOM (denoted as QMOM-Radau in the remainder of this paper) changes to

$$\int_0^\infty f(V)n(V)dV \approx w_1 f(V_1) + \sum_{\alpha=2}^{N_V} w_\alpha f(V_\alpha). \tag{18}$$

In order to fix an abscissa in the moment inversion process, the recursion coefficient a_{N_V-1} is chosen in such a way that V_1 is a root of the orthogonal polynomial $P_{N_V}(V)$:

$$P_{N_V}(V_1) = 0. \tag{19}$$

According to Eq. (15), this leads to

$$(V_1 - a_{N_V-1})P_{N_V-1}(V_1) - b_{N_V-1}P_{N_V-2}(V_1) = 0, \tag{20}$$

and

$$a_{N_V-1} = V_1 - b_{N_V-1}\frac{P_{N_V-2}(V_1)}{P_{N_V-1}(V_1)}. \tag{21}$$

As a result, V_1 is an eigenvalue of the Jacobian (see Eq. (17)) and therefore it is found as a quadrature node. Further details on Gauss-Radau quadrature can be found in [55].

2.1.3. Extended QMOM

The general advantage of the recently developed EQMOM approach [1] over standard QMOM is that the NDF is approximated using kernel density functions instead of Dirac delta functions (cf. Eq. (10))

$$n\left(\tilde{V}\right) \approx \sum_{\alpha=1}^{N_V} w_\alpha \delta_\sigma\left(\tilde{V};\tilde{V}_\alpha\right), \tag{22}$$

where the additional parameter σ, which represents the scale parameter of the kernel density functions, is required. Thereby, a new coordinate $\tilde{V}$ is introduced, which is defined as follows:

$$\tilde{V} = V - V_1, \tilde{V} \in [0,\infty]. \tag{23}$$

This transformation is needed as Γ-distributions, which are defined on the interval for $\tilde{V}$, are used for the kernel density functions:

$$\delta_\sigma\left(\tilde{V};\tilde{V}_\alpha\right) = \frac{\tilde{V}^{\frac{\tilde{V}_\alpha}{\sigma}-1}e^{-\tilde{V}/\sigma}}{\Gamma\left(\frac{\tilde{V}_\alpha}{\sigma}\right)\sigma^{\frac{\tilde{V}_\alpha}{\sigma}}}. \tag{24}$$

Here, $\tilde{V}_\alpha$ is the position of the Γ-distribution corresponding to node α and $\Gamma\left(\tilde{V}_\alpha,\sigma\right)$ is the gamma function. The k-th moment of a Γ-distribution is obtained multiplying Eq. (24) by $\tilde{V}^k$ and integrating over the whole phase space:

$$\tilde{m}_{\Gamma,k} = \frac{\Gamma\left(\frac{\tilde{V}_\alpha}{\sigma}+k\right)}{\Gamma\left(\frac{\tilde{V}_\alpha}{\sigma}\right)}\sigma^k. \tag{25}$$

Therefore, the transformation of Eq. (22) into moment equations leads to

$$\tilde{m}_k = \sum_{\alpha=1}^{N_V} w_\alpha \frac{\Gamma\left(\frac{\tilde{V}_\alpha}{\sigma}+k\right)}{\Gamma\left(\frac{\tilde{V}_\alpha}{\sigma}\right)}\sigma^k, \tag{26}$$

where $\tilde{m}_k$ represents the transported moments of the soot particle distribution transformed to the support interval of Γ-distributions. This transformation step needs to be done at the beginning of each EQMOM moment inversion step as the lower boundary of the integration interval of the physical soot distribution moments is given by the volume of the smallest particle V_1 (cf. Eq. (22)

$$V \in [V_1,\infty], \tag{27}$$

whereas Γ-distributions are defined for the interval $\tilde{V} \in [0,\infty]$ (cf. Eq. (24)). A reconstructed NDF based on a sum of Γ-distributions would therefore contain unphysical volumes as small as zero. The rule to transform m_k to $\tilde{m}_k$ builds upon the idea of shifting the physical soot particle distribution leftwards by the value of V_1 [78] (cf. Eq. (23)) in order to perform the moment inversion and NDF reconstruction process in a consistent manner:

$$\begin{aligned}\tilde{m}_k &= \int_{V_1}^\infty \tilde{V}(V)^k n(V)dV = \int_{V_1}^\infty \left(\sum_{r=0}^{k}\binom{k}{r}V^{k-r}(-V_1)^r\right)n(V)dV \\ &= \sum_{r=0}^{k}\binom{k}{r}m_{k-r}(-V_1)^r.\end{aligned} \tag{28}$$

It should be mentioned that a similar moment transformation strategy has been used by Vikas et al. [49], who applied EQMOM to model radiation transport.

Eq. (26) can then be simplified to

$$\begin{aligned}\tilde{m}_k &= \sum_{\alpha=1}^{N_V} w_\alpha \tilde{V}_\alpha^k + \sum_{\alpha=1}^{N_V} w_\alpha P_{k-1}\left(\tilde{V}_\alpha,\sigma\right) \\ &= \tilde{m}_k^* + \sum_{\alpha=1}^{N_V} w_\alpha P_{k-1}\left(\tilde{V}_\alpha,\sigma\right),\end{aligned} \tag{29}$$

where $P_{k-1}\left(\tilde{V}_\alpha,\sigma\right)$ is a homogeneous polynomial. In order to determine the scale parameter σ, an additional moment needs to be transported, which is used to determine the value of σ.[1] The scale parameter is found iteratively, by choosing a value for σ and solving Eq. (29). These steps are repeated until the condition

$$\tilde{m}_{2N_V} - \tilde{m}_{2N_V}^* - \sum_{\alpha=1}^{N_V} w_\alpha P_{2N_V-1}\left(\tilde{V}_\alpha,\sigma\right) = 0 \tag{30}$$

is fulfilled. As demonstrated by Yuan et al. [1], this iterative solution process is a root-finding problem, where σ is found by applying a combination of a secant method and a bisectional method. Having found the set of nodes $\tilde{V}_\alpha$, weights w_α and σ, for which Eq. (30) is satisfied, an additional step is conducted before the source terms are evaluated. Unlike the case of QMOM, the nodes and weights are not directly used to evaluate the moment source terms, but

[1] $2N_V + 1$ moments instead of $2N_V$ moments as in QMOM.

additional weights and nodes, denoted as second Gaussian quadrature nodes $\tilde{V}_{\alpha,\epsilon}$ and weights $\tilde{w}_{\alpha,\epsilon}$,

$$\tilde{V}_{\alpha,\epsilon} \in [0,\infty], \tag{31}$$
$$\tilde{w}_{\alpha,\epsilon} \in [0,1], \tag{32}$$

are evaluated for each Γ-distribution. At this point, the advantage of choosing Γ-distributions becomes evident. The definition of a Γ-distribution is equivalent to the weight function of Laguerre polynomials [55]

$$w(s) = s^{\eta}e^{-s}, \quad \eta > -1, \tag{33}$$

where the recursion coefficients a_γ and b_γ (cf. Eq. (15)) are given by analytical expressions:

$$\begin{aligned} a_\gamma &= 2\gamma + \eta + 1 \\ b_0 &= \Gamma(1+\eta) \\ b_\gamma &= \gamma(\gamma+\eta), \quad \gamma \geqslant 1. \end{aligned} \tag{34}$$

In contrast to Eq. (16), Eq. (34) is independent from the number of transported moments, so the dimension of the Jacobian (see Eq.(17)) and therefore the amount of second Gaussian quadrature nodes N'_V can be chosen arbitrarily. The number of transported moments determines the amount of Γ-distributions which are used to describe the soot particle NDF. To represent not only unimodal but also bimodal particle distributions in flames and combustion systems, the choice of two Γ-distributions to approximate the NDF appears to be intuitive and is made in this study. Before the physical source terms are evaluated, the reconstructed distribution represented discretely by the sum of the second Gaussian quadrature nodes is shifted back to the physical interval (Eq. (23)) applying

$$V_{\alpha,\epsilon} = \tilde{V}_{\alpha,\epsilon} + V_1, \tag{35}$$
$$w_{\alpha,\epsilon} = \tilde{w}_{\alpha,\epsilon}. \tag{36}$$

These aspects lead to the following formulation of the EQMOM source terms (again shown for the coagulation term only):

$$\begin{aligned} \dot{m}_{k,coag} = &\frac{1}{2}\sum_{i=1}^{N_V}\sum_{m=1}^{N'_V}\sum_{j=1}^{N_V}\sum_{n=1}^{N'_V} w_i w_{i,m} w_j w_{j,n} \beta\left(V_{i,m}, V_{j,n}\right) \\ &\left[\left(V_{i,m}+V_{j,n}\right)^k - V_{i,m}^k - V_{j,n}^k\right]. \end{aligned} \tag{37}$$

2.1.4. CQMOM

The Conditional Method of Moments (CQMOM) [2] allows to solve the moments of a multivariate NDF by finding the weights and abscissas of the second internal coordinate conditioned on nodes of the first coordinate. In this paper, CQMOM is used to characterize soot particles both by their volume V and their surface S to consider aggregation. Therefore, the bivariate NDF is represented by

$$n(V,S) = n_V(V) n_{SV}(S|V) \approx \sum_{\alpha=1}^{N_V}\sum_{\beta=1}^{N_S} w_\alpha w_{\alpha,\beta} \delta(V - V_\alpha)\delta\left(S - S_{\alpha,\beta}\right), \tag{38}$$

and the bivariate moments are written as

$$m_{k,l} = \int_0^\infty \int_0^\infty V^k S^l n(V,S) dV dS = \sum_{\alpha=1}^{N_V}\sum_{\beta=1}^{N_S} w_\alpha w_{\alpha,\beta} V_\alpha^k S_{\alpha,\beta}^l, \tag{39}$$

with the N_S conditioned surface nodes $S_{\alpha,\beta}$ and weights $w_{\alpha,\beta}$. Since the sum of the weighted, conditioned nodes represents the conditional moments, $A_{\alpha,l}\left(S_{\alpha,\beta}, w_{\alpha,\beta}\right)$

$$m_{k,l} = \sum_{\alpha=1}^{N_V}\sum_{\beta=1}^{N_S} w_\alpha w_{\alpha,\beta} V_\alpha^k S_{\alpha,\beta}^l = \sum_{\alpha=1}^{N_V} w_\alpha V_\alpha^k A_{\alpha,l}(S_{\alpha,\beta}, w_{\alpha,\beta}), \tag{40}$$

the bivariate moment inversion problem is simplified to two consecutive quasi-univariate moment inversion steps. To achieve this, the pure volume moments $m_{k,0}$ are first inverted to compute the N_V nodes and weights for the volume direction V_α and w_α. Then, the conditional moments are evaluated, solving the following linear system shown here for $l = 1$:

$$\begin{bmatrix} A_{1,1} \\ \vdots \\ A_{N_V,1} \end{bmatrix} = \begin{bmatrix} V_1^0 & \cdots & V_{N_V}^0 \\ & \vdots & \\ V_1^{N_V-1} & \cdots & V_{N_V}^{N_V-1} \end{bmatrix}^{-1} \begin{bmatrix} w_1 & 0 & 0 \\ 0 & \ddots & 0 \\ 0 & 0 & w_{N_V} \end{bmatrix}^{-1} \begin{bmatrix} m_{0,1} \\ \vdots \\ m_{N_V-1,1} \end{bmatrix}. \tag{41}$$

The conditional moments are then inverted following Eq. (40) to find the N_S conditioned weights and nodes $w_{\alpha,\beta}$ and $S_{\alpha,\beta}$.

Finally, the bivariate moment source terms are closed using the nodes and weights of both directions. This is demonstrated again for the coagulation term [54]:

$$\begin{aligned} \dot{m}_{k,coag} = &\int_0^\infty \int_0^\infty V^k S^l \Bigg[\frac{1}{2}\int_0^S \int_0^V \beta(V-V', V', S-S', S') \\ &n(V-V', S-S') n(V', S') dV' dS' - \int_0^\infty \int_0^\infty \beta(V, V', S, S') \\ &n(V,S) n(V', S') dV' dS'\Bigg] dV dS \\ = &\frac{1}{2}\sum_{i=1}^{N_V}\sum_{m=1}^{N_S}\sum_{j=1}^{N_V}\sum_{n=1}^{N_S} w_i w_{i,m} w_j w_{j,n} \beta\left(V_i, S_{i,m}, V_j, S_{j,n}\right) \\ &\left[\left(V_i+V_j\right)^k \left(S_{i,m}+S_{j,n}\right)^l - V_i^k S_{i,m}^l - V_j^k S_{j,n}^l\right]. \end{aligned} \tag{42}$$

2.1.5. Combination of EQMOM/CQMOM

The combination of EQMOM and CQMOM yields a moment method which offers the benefits of having both a continuous reconstructed NDF and considering a bivariate description of soot particles. Substituting the Dirac delta functions for the volume space in Eq. (38) by kernel density functions yields

$$n\left(\tilde{V}, S\right) \approx \sum_{\alpha=1}^{N_V}\sum_{\beta=1}^{N_S} w_\alpha w_{\alpha,\beta} \delta_\sigma\left(\tilde{V}; \tilde{V}_\alpha\right)\delta\left(S - S_{\alpha,\beta}\right), \tag{43}$$

and Eq. (39) changes to

$$m_{k,l} = \int_0^\infty \int_0^\infty V^k S^l n(V,S) dV dS = \sum_{\alpha=1}^{N_V}\sum_{\beta=1}^{N_S} w_\alpha w_{\alpha\beta} m_{V,k}^{(\alpha)} S_{\alpha\beta}^l, \tag{44}$$

where the moments of the N_V Γ-distributions $m_{V,k}^{(\alpha)}$ are given by Eq. (25) taking into account the necessary transformation step described above.

These modifications yield changes in the linear system of Eq. (41):

$$\begin{bmatrix} A_{1,1} \\ \vdots \\ A_{N_V,1} \end{bmatrix} = \begin{bmatrix} m_{V,0}^{(1)} & \cdots & m_{V,0}^{(N_V)} \\ & \vdots & \\ m_{V,N_V-1}^{(1)} & \cdots & m_{V,N_V-1}^{(N_V)} \end{bmatrix}^{-1} \begin{bmatrix} w_1 & 0 & 0 \\ 0 & \ddots & 0 \\ 0 & 0 & w_{N_V} \end{bmatrix}^{-1} \begin{bmatrix} m_{0,1} \\ \vdots \\ m_{N_V-1,1} \end{bmatrix}. \tag{45}$$

However, the solution procedure of the combined EQMOM/CQMOM approach is similar to CQMOM. First, EQMOM is applied to invert the univariate volume moments $m_{k,0}$. The abscissas $\tilde{V}_\alpha$, weights w_α and the scale parameter σ are used to compute the moments of the Γ-distributions $\tilde{m}_{V,k}^{(\alpha)}$, which are first transformed to the physical space leading to $m_{V,k}^{(\alpha)}$ and then used to solve the linear system

given in Eq. (45). The abscissas $S_{\alpha,\beta}$ and weights $w_{\alpha,\beta}$ are found by inverting the conditional moments $A_{\alpha,l}(S_{\alpha,\beta}, w_{\alpha,\beta})$.

The closure of the ECQMOM source term is similar to Eq. (42) adding additional loops for the second Gaussian quadrature volume nodes. As these formulations are straightforward, the ECQMOM coagulation source term is not shown here for brevity.

2.2. Monte Carlo

As mentioned before, MC can reconstruct the NDF very accurately. Thus, similar to previous studies, where the numerical results of moment methods are compared to MC results [34,45], we perform MC simulations for the particle modeling test flames discussed in Section 2.4 using the MC tool *Sweep2* [56]. The results are used as an additional reference to validate the moment-based approaches described in Section 2.1. In Sweep2, soot is represented by an ensemble of stochastical particles. This ensemble is adapted according to the probability that an ensemble-changing event will happen as a function of the height above the burner (HAB). This method is realized using the *Linear Process Deferment Algorithm* [11] to optimize the computational efficiency. Further details on the underlying algorithmic methods can be found in [6,9,11].

2.3. Physical and chemical models

The gas phase of the burner-stabilized premixed test flames studied is simulated using the flame solver package OpenSMOKE [79]. Species diffusion is modeled using the mixture-averaged diffusion model. Thermal diffusion (Soret effect) is considered in the species transport equations. The solution gradient and curvature are controlled to ensure the smoothness of the calculated profiles. The QMOM-based solvers are integrated into OpenSMOKE in order to directly couple the solid and the gas phase. This coupling process enables the correction of relevant gaseous species profiles due to their transition to the solid phase as a result of nucleation, condensation and HACA surface growth.

2.3.1. Gas phase

The detailed gas phase model, which is attached as supplementary material, is a subset of a larger kinetic scheme available on the web.[2] It includes only the high temperature sub-mechanism and accounts for 170 species and about 5500 reactions. The scheme is based on a detailed description of the C_1–C_4 chemistry, which has been extensively validated in comparison with a large amount of experimental data [57]. It includes detailed models of the formation and disappearance of first aromatic rings (benzene (A1-C_6H_6) and toluene (A1-C_7H_8), in particular) and of PAHs, which are known to be precursors of soot.

The formation of the first aromatic rings has been carefully validated in recent studies. In this context, the capability of the model to describe the pyrolysis and oxidation of A1-C_6H_6 has been validated in different laminar flames with different fuels [58]. Special focus was put on the first ring formation by C_2 and C_4 chemistry and by the resonantly stabilized radicals such as propar-gyl (C_3H_3) and cyclopentadienyl (C_5H_5) [60,61].

The growth rates of larger PAH species are modeled using the well-known HACA mechanism [80]. The kinetic scheme includes also the typical reaction pathways of chemistry of PAH growth, like the stabilized radical mechanisms, even though they are of lower importance in the case of ethylene flames. The main consumption reactions of aromatics and PAHs are H abstraction reactions by H and OH radicals. The capability of the model to reproduce PAH formation and disappearance is of paramount importance for the prediction of the soot formation. For this reason, the mechanism was already discussed and extensively validated, as reported in the referred literature [58–61]. To specifically adapt the kinetic scheme to be connected to the method of moments, A4-$C_{16}H_{10}$ is set to be the heaviest component of the gas phase and thus accounts for other heavier PAHs.

2.3.2. Solid phase

The formulation of the physical and chemical source terms (cf. Eq. (2)) follows previous studies, e.g., [12,29,39]. Therefore, only a short outline is given here. It is important to mention that the formulations of the physical and chemical rates are the same for both the Monte Carlo code and the QMOM-based solvers.

In order to describe soot particle nucleation, different models are available in the literature as the process of nucleation is not yet fully understood [81]. Hence, frequently applied nucleation models assume a dimerization reaction of PAH dimers [34,39,45,74], a chemical lumping process [25,26] or a A4-$C_{16}H_{10}$ dimerization reaction [12,29,33,82,83] leading to the first solid particles. In this study we apply the A4-$C_{16}H_{10}$ dimerization model to describe the nucleation rate of the smallest soot particles pre-sent in the system.

Coagulation is described using the Smoluchowski equation, where the transition between the continuum and the free molecular regime kernel is accounted for by applying a harmonic mean interpolation of the collision frequencies of the two regimes [84]. The collision diameter d_c is evaluated following Kruis et al. [85]

$$d_c = d_p n_p^{1/D_f}, \tag{46}$$

where the fractal dimension D_f is kept constant at $D_f = 1.8$. As the number of primary particles n_p in the univariate methods is fixed at $n_p = 1$, the collision diameter is equal to the primary particle diameter d_p. The bivariate models assume that aggregating particles are linked by point contacts and all primary particles of an aggregate have the same diameter. Therefore, the correlation between the internal coordinates (V, S) and the aggregate properties d_p and n_p is given by Blanquart and Pitsch [39]

$$V = \frac{\pi}{6} n_p d_p^3, \tag{47}$$

$$S = \pi n_p d_p^2. \tag{48}$$

Particle surface growth is considered to happen through condensation of A4-$C_{16}H_{10}$ and the H-abstraction-C_2H_2-addition (HACA) mechanism [24]. The formulation of the condensation rate is based on the Smoluchowski equation for the collision of A4-$C_{16}H_{10}$ with soot. In contrast, the formulation of the HACA reaction rate is based on a heterogeneous Arrhenius approach [28,86]. The HACA rates are taken from [29].

Details with respect to the formulation of the presented source terms within the QMOM framework can be found in Blanquart [75] who applied a slightly different nucleation and condensation model (nucleation through dimerization of two PAH dimers instead of dimerization of two PAH molecules, condensation of PAH dimers instead of condensation of PAH molecules). Therefore, in our model, we substituted the dimer properties needed in the QMOM-based equations in [75] by A4-$C_{16}H_{10}$ properties.

2.4. Experimental setup

As mentioned above, three burner-stabilized premixed ethylene flames are considered as reference cases to validate the numerical models.

First, a $C_2H_4/O_2/Ar$ flame with an equivalence ratio of $\phi = 3.06$, which was studied by Castaldi et al. [62] experimentally, is chosen

[2] http://creckmodeling.chem.polimi.it.

as the reference flame to validate the kinetic gas phase model. Several measured PAH species profiles are available, which were sampled using an online gas chromatograph/mass spectrometer analysis technique [62]. As the significant heat losses are difficult to estimate in premixed burner-stabilized flames (e.g., [39]), the temperature profile measured is used as an input in the numerical simulations. In order to validate the kinetic model's ability to predict the effect of methane (CH_4) addition on the formation of soot precursors, the laminar flow reactor experiments of Roesler et al. [63] are also modeled. This involves studying CH_4/C_2H_4 mixtures in a laminar flow reactor at $T = 1430$ K. Initially, the fuel consists of pure C_2H_4. Then, CH_4 is gradually added to the system, maintaining the total carbon content (3 mol-%) and a C/O ratio of about 2, corresponding to an equivalence ratio of between $\phi = 6 - 7$ due to the added H_2 in the presence of CH_4. Finally, the model is vali-dated against several measurements regarding its ability to repro-duce the flame speed in $C_2H_4/O_2/N_2$ flames at different pressures and compositions [64–68].

In order to validate the statistical soot models EQMOM and ECQMOM two test flames are chosen. The first flame which is chosen for the validation of the soot model is a $C_2H_4/O_2/Ar$ flame, which was studied experimentally by Abid et al. [69]. It has an equivalence ratio of $\phi = 2.07$ and a cold gas velocity of $u_0 = 6.53$ cm/s. The experimental setup included measurements of the particle size distribution using a scanning mobility particle sizer (SMPS) and transmission electron microscopy (TEM) measurements to study the morphology of the particles [69]. The TEM experiments indicated that this flame does not tend to build aggregates and therefore particle volume and surface can be treated as dependent coordinates applying a univariate coalescence model. Hence, this flame is chosen as a benchmark flame to model soot evolution with the univariate soot models introduced in Section 2.1. For the same reasons as mentioned above, the temperature profile measured by Abid et al. [69] is used in the simulation.

In order to validate the bivariate models, a third test flame is chosen, where aggregation is important. TEM measurements on a $C_2H_4/O_2/N_2$ flame with $\phi = 2.64$ and $u_0 = 6.84$ cm/s revealed [70] that aggregation is a major process in this flame. A previous numerical study of this flame revealed that the assumption of a pure aggregation model predicts the measured mean soot quantities very well [45,87]. Therefore, the flame serves as a suitable test case for the bivariate models introduced in Section 2.1 considering the case of pure aggregation. It should be mentioned that this flame is listed as one of the target flames of the International Sooting Flame Workshop (ISF) and has already been modeled in other studies [34,39,45,74]. The temperature is again fixed in the simulations applying the temperature profile suggested on the ISF website [88].

As all test flames considered are based on C_2H_4, it should be mentioned that the models described have no restrictions regarding their applicability to other fuels.

3. Results

In this section, the kinetic gas phase model, the univariate EQMOM and the bivariate ECQMOM model are validated against experiments. Furthermore, the soot models are compared to MC simulations and the other univariate and bivariate moment methods explained in Section 2.

3.1. Evaluation of the kinetic gas phase model

As mentioned in Section 2.4, the experimentally measured temperature profile is used in the simulation. Thereby, this profile is increased by $\Delta T = 100$ K in the post-flame zone to better reproduce the post-flame values of several important stable species, such as C_2H_2, H_2 and CO. This correction is expected to be within the experimental uncertainty range of temperature measurements in sooting flame conditions, as the flame temperature measured could be affected by the soot deposition on the thermocouple [89,90]. Figure 1 shows the comparison between the measured and the simulated mole fraction profiles for the major species as well as the PAHs. Taking into account the fact that species mea-surements in sooting flames are difficult and therefore yield to uncertainties, the comparison between the model predictions and the measurements is quite satisfactory. This applies not only for the general flame structure and the major gaseous products, but also for the intermediate species and aromatic compounds with 1–4 rings. The major deviation refers to toluene. Part of the toluene overestimation is related to the benzene overestimation. This error is not present in the case of the laminar flow reactor (Fig. 2a), where the agreement between the model and the experi-mental data is better. Moreover, toluene predictions are generally quite satisfactory in other comparisons, where the presence of large or systematic deviations cannot be observed [61].

One of the main purposes of the mechanism is to precisely describe the A4-$C_{16}H_{10}$ profile, which directly influences the nucleation and the condensation rate of the soot model. As mentioned, A4-$C_{16}H_{10}$ is mainly built by HACA reactions, where phenylacetylene ($C_6H_5C_2H$) is a key intermediate. As shown in Fig. 1d, the model is able to represent the measured $C_6H_5C_2H$ trend very well. Consequently, the kinetic model is also able to predict the measured A4-$C_{16}H_{10}$ profile well.

The comparison between the model and experiments regarding the effect of CH_4 addition is shown in Fig. 2a. The simulation results for premixed mixtures in a flow reactor are reported as a function of a mixture parameter β, representing the fraction of fuel carbon injected as methane [59]:

$$\beta = \frac{X_{CH_4}}{X_{CH_4} + X_{C_2H_4}}, \tag{49}$$

where X_i is the mole fraction of species i. In this case, the model also correctly predicts the experimental trends, especially the significant increase in benzene when CH_4 is added to the system. Similarly, the same kinetic model proved able to properly estimate the formation of benzene and larger aromatics in a coflow diffusion flame fed with mixtures of C_2H_4 and CH_4 [59]. Finally, the flame speed simulations and measurements at different equivalence ratios and pressures are shown in Fig. 2b. It can be observed that the kinetic model is able to reproduce the flame speed of C_2H_4 flames correctly over a wide range of equivalence ratios and at different pressures.

3.2. Evaluation of the univariate EQMOM model

As mentioned, the burner-stabilized, premixed $C_2H_4/O_2/Ar$ flame which was studied experimentally by Abid et al. [69] is chosen as the reference flame for the univariate EQMOM model. Figure 3 shows a comparison between the experimental results [69] and the EQMOM results. As already mentioned in Section 2.1.3, two Γ-distributions are chosen to approximate the NDF. The source terms are evaluated using 100 second Gaussian quadrature nodes (50 nodes per Γ-distribution). Very good agree-ment is found for the soot volume fraction f_v. On the other hand, the total particle number density N is overpredicted by the model, taking into account the full NDF. However, the overprediction of the particle number density in comparison to SMPS results is expected, since the SMPS technique is not capable of probing the smallest soot particles. The lower detection size limit in the study by Abid et al. [69] is reported to be $d = 2.5$ nm. In order to ensure

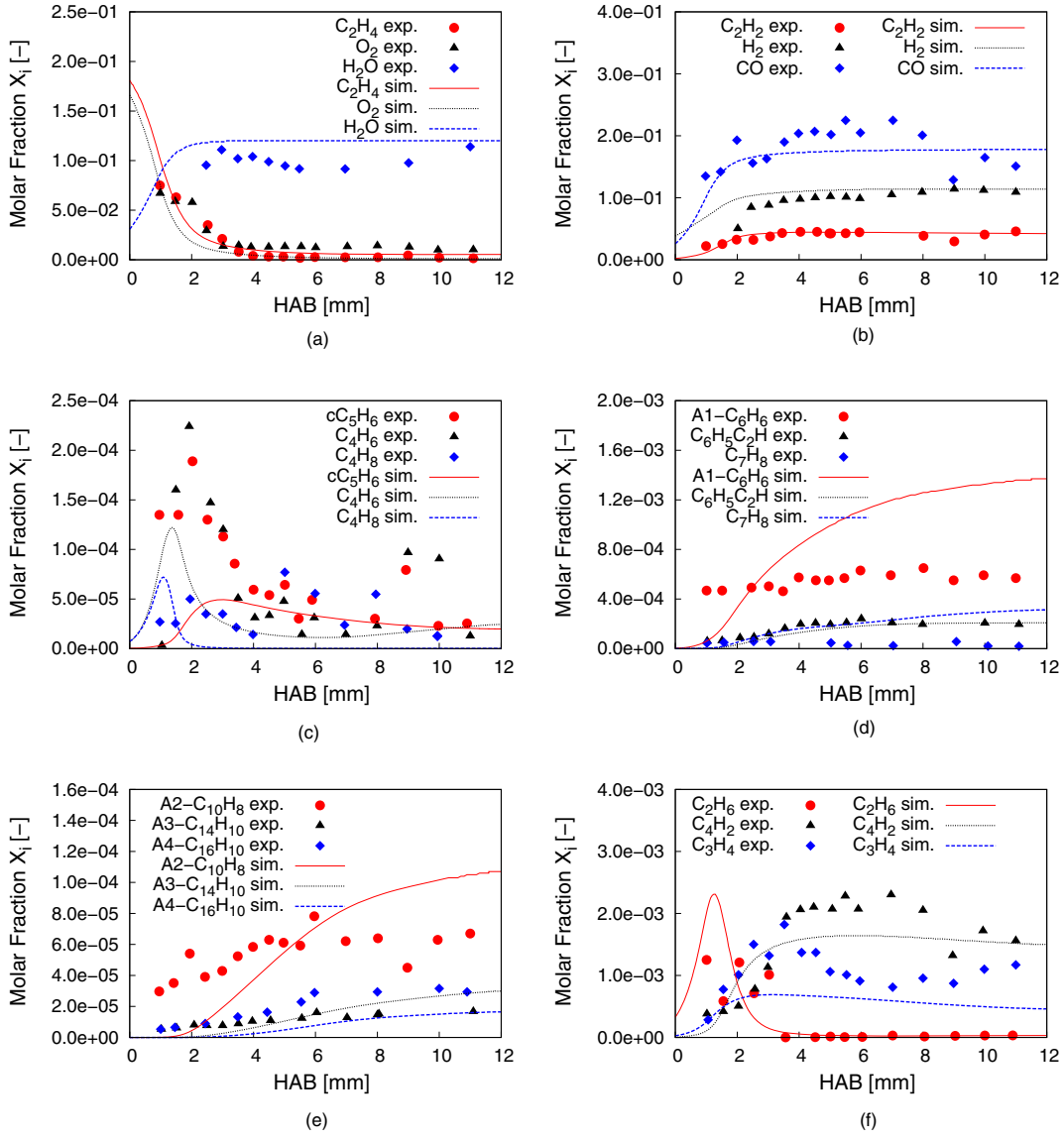

Fig. 1. Comparison between experimental and calculated mole fraction profiles for major species and PAHs in a premixed C_2H_4/O_2/Ar flame with $\phi = 3.06$ [62]. (a) C_2H_4, O_2, H_2O. (b) C_2H_2, H_2, CO. (c) cC_5H_6, C_4H_6, C_4H_8. (d) A1-C_6H_6, $C_6H_5C_2H$, C_7H_8. (e) A2-$C_{10}H_8$, A3-$C_{14}H_{10}$, A4-$C_{16}H_{10}$. f) C_2H_6, C_4H_2, C_3H_4.

comparability, these smallest particles are subtracted from the EQMOM solution. The same procedure was carried out by Zhao et al. [91] in a MC simulation of an ethylene flame, which was investigated experimentally using a SMPS setup. Since EQMOM offers a reconstructed NDF, this clipping step can be realized as accurately as in a MC method. As shown in Fig. 3b, this leads to good agreement between the measured and the modeled particle number density.

The comparison between the results obtained with EQMOM, QMOM, QMOM-Radau and MC is shown in Fig. 4. Both the QMOM and the QMOM-Radau source terms are evaluated using three quadrature nodes. More quadrature nodes do not lead to any further improvements in the solution of the case studied. As mentioned above, two Γ-distributions with 100 second Gaussian quadrature nodes are used in EQMOM. The results show only small deviations for f_v among the models. However, regarding the total number density N, both quantitative and qualitative differences can be seen. While EQMOM and QMOM-Radau are able to reproduce the history of the number density towards higher HABs and the two compare well to MC, QMOM overpredicts the total particle number. More precisely, it fails to capture the steep gradient of the number density as a function of the HAB. Therefore, the deviations quickly reach a factor of two (at about HAB = 10 mm). The differences increase further at higher HABs, where QMOM predicts too slight a decrease in N in comparison to MC.

The reason for this effect is further analyzed by looking at the source terms of the zeroth moment m_0, which represents N. In the present study, m_0 is only influenced by the processes of nucle-ation and coagulation. Since nucleation is independent from the NDF, the deviations originate mainly in the coagulation source term (cf. Eqs. (9) and (37)). Figure 5 shows the relative deviations of the QMOM and the QMOM-Radau coagulation source term with respect to m_0 from EQMOM as a function of the HAB. Both QMOM and QMOM-Radau yield differences of approximately 5% at about HAB = 5 mm. However, these differences stay almost constant or grow even larger in QMOM, whereas the relative deviation of QMOM-Radau from EQMOM declines in later parts of the flame. The consistent rate differences in QMOM lead to the deviations mentioned for N.

The underlying effect can be explained as follows. As shown in Section 2, the principle of evaluating nodes and weights based on a transported set of moments, and using these nodes to close the

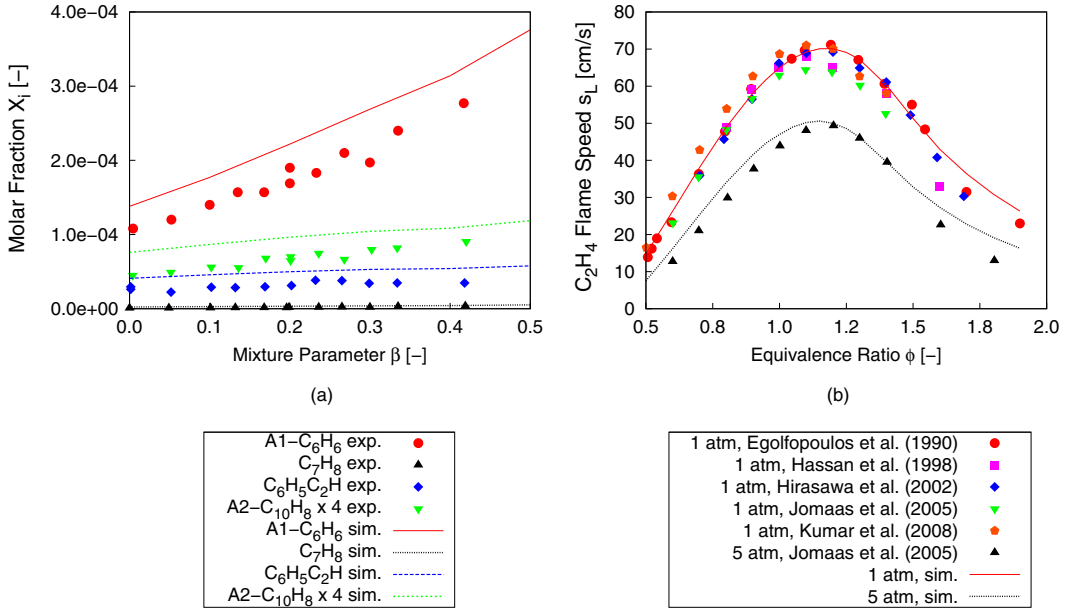

Fig. 2. Comparison between experimental and modeling results regarding the effect of CH_4 addition and the laminar flame speed s_L at different equivalence ratios and pressures in C_2H_4 flames. (a) Mole fraction of A1-C_6H_6, C_7H_8, $C_6H_5C_2H$ and A2-$C_{10}H_8$ (times 4) in a laminar flow reactor for the combustion of C_2H_4 and C_2H_4/CH_4 mixtures at $T = 1425$ K as a function of the mixture parameter β [63]. (b) Simulated and measured ([64–68]) flame speed s_L at $p = 1$ atm and $p = 5$ atm for different equivalence ratios ϕ.

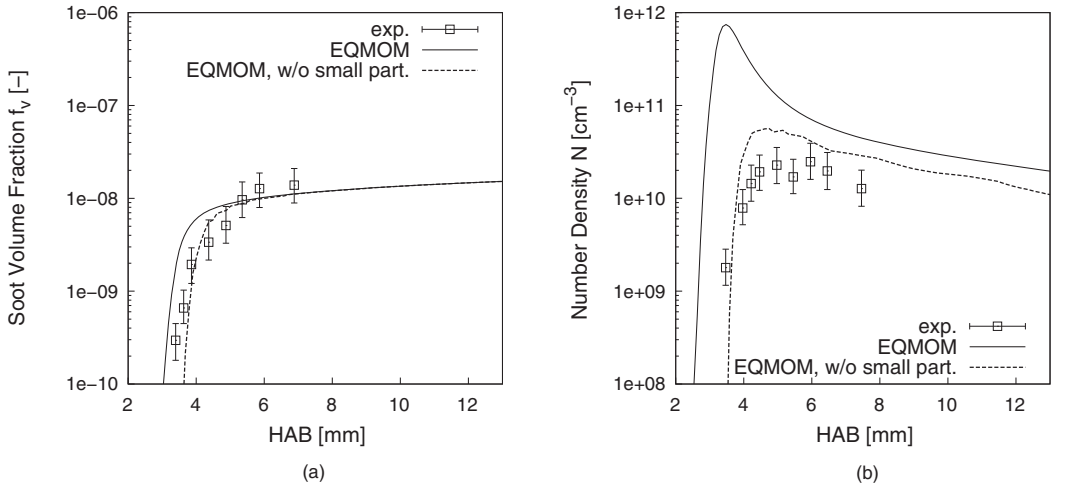

Fig. 3. Comparison between the EQMOM model and experiments for a burner-stabilized premixed $C_2H_4/O_2/Ar$ with $\phi = 2.07$ [69]. (a) Soot volume fraction f_v. (b) Total particle number density N. Also, the EQMOM result is adjusted to the experimentally accessible particle size (dashed line).

source terms, applies to all QMOM-based approaches. Therefore, it seems straightforward that the differences correlate with the position and the weights of the calculated quadrature nodes. In order to analyze how the coagulation rate of m_0 depends on the specific quadrature nodes, the NDF from EQMOM is used to investigate the size dependency of the coagulation source term. Thereby, the particle size spectrum is divided into two bins, Bin1 and Bin2, respectively. The limit between Bin1 and Bin2 is set at dp = 4 nm. The evaluation of the coagulation rate is now split into three different events: Bin1-Bin1, Bin1-Bin2 and Bin2-Bin2 collisions. The rates are normalized by the total coagulation rate. The result is shown in Fig. 6. Obviously, collisions among Bin1 particles are only important at lower HABs, since particles larger than dp = 4 nm are not yet formed in this part of the flame. At higher HABs, the presence of Bin2 particles leads to Bin2-Bin2 collisions contributing significantly to the overall coagulation rate. However, especially at high HABs, Bin1-Bin2 collisions are the most dominant process contributing to the coagulation rate. That implies that the smallest soot particles need to be represented accurately by the statistical model at all HABs to describe the dynamics of the coagulation process properly. As mentioned in Section 2.1.1, the position of the nodes is not fixed in QMOM, but is instead determined by the roots of orthogonal polynomials, which are evaluated by the transported moment set. Figure 7, showing the position and weight of the EQMOM, QMOM and QMOM-Radau quadrature nodes at two HABs, reveals that QMOM does not place any interpolation node to the size region of the smallest soot particles at higher HABs. As a consequence, QMOM cannot describe the amount of the smallest particles accurately. This conclusion is supported by the results of the QMOM-Radau method, where one quadrature node is fixed at the position of the smallest particles. This specific inter-polation node for the small particles ensures that QMOM-Radau captures the decline in the number density in the post-inception zone much better than QMOM, see Fig. 4. The non-fixed quadrature

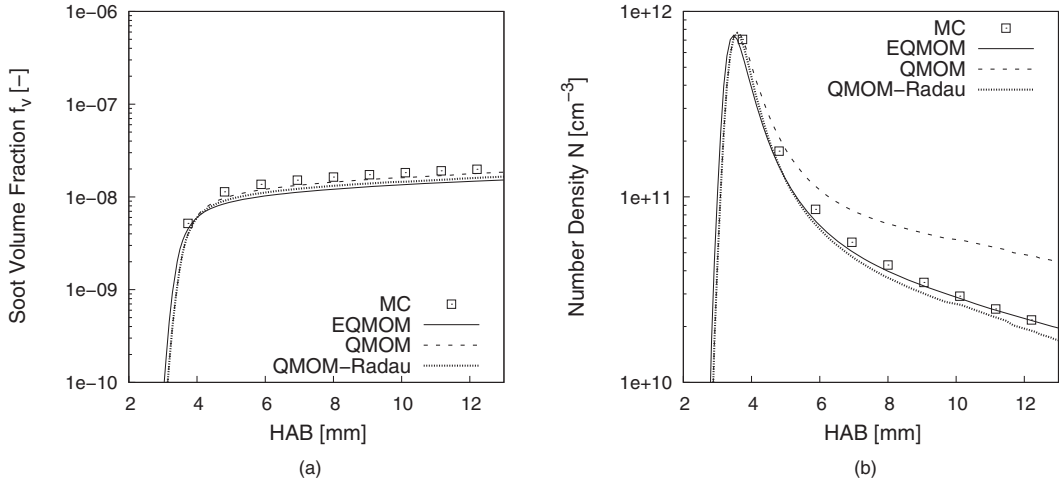

Fig. 4. Comparison between the EQMOM, QMOM, QMOM-Radau and MC approaches for the burner-stabilized premixed $C_2H_4/O_2/Ar$ test flame with $\phi = 2.07$ [69]. (a) Soot volume fraction f_v. (b) Total particle number density N.

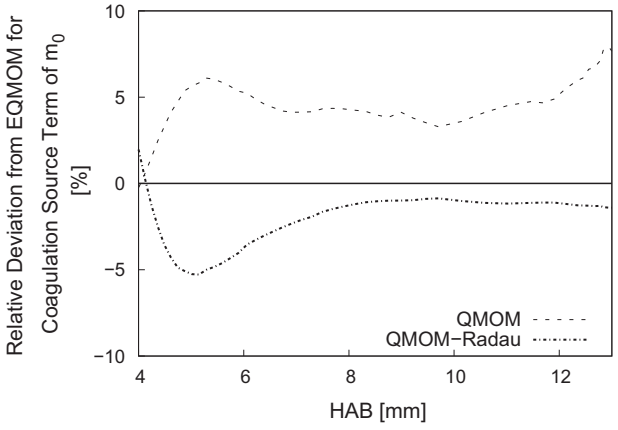

Fig. 5. Relative deviations of the simulated coagulation source term of the zeroth moment m_0 of QMOM and QMOM-Radau with respect to EQMOM for the $C_2H_4/O_2/Ar$ test flame with $\phi = 2.07$ [69] as a function of the HAB.

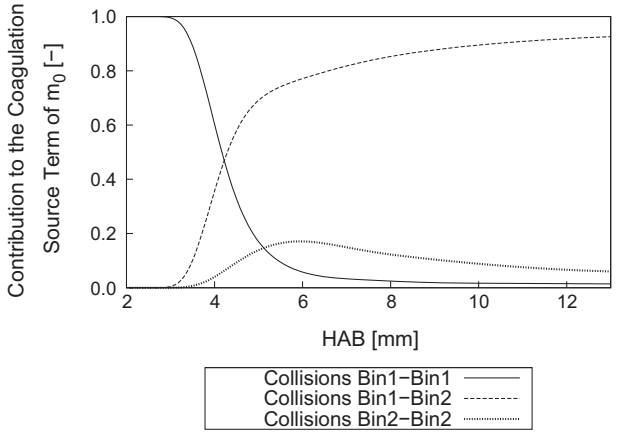

Fig. 6. Contribution of Bin1-Bin1, Bin2-Bin2 and Bin1-Bin2 collisions to the coagulation source term of the zeroth moment m_0 using the EQMOM model for the simulation of the $C_2H_4/O_2/Ar$ test flame with $\phi = 2.07$ [69].

nodes are positioned at large particle diameters in order to describe the shape of the second size mode.

The permanent presence of an interpolation node in the region of the smallest particles is also achieved in EQMOM, see Fig. 7. Based on the discussion above, it is not surprising that a numerical method which reconstructs the whole NDF is able to close the source terms accurately. However, the good agreement between EQMOM and MC in Fig. 4 also implies that the choice of only two Γ-distributions to reconstruct the NDF is sufficient to approximate a bimodal soot ensemble. Therefore, only $2N_V + N_\sigma$ (N_V=2) moments of the distribution need to be transported. The same number of moments enables the evaluation of three Gaussian Quadrature nodes in QMOM or QMOM-Radau. However, EQMOM utilizes the known moments more efficiently, as it enables the reconstruction of the continuous NDF.

It is interesting to note that the importance of the smallest particles and the impact on solution methods was previously expressed by Mueller et al. [45], who compared different moment methods to MC results. It was found that BiMOMIC [34] is not able to capture the particles of the first mode. Therefore, the method was expanded to create the Hybrid Method of Moments (HMOM) by introducing a Dirac delta representation of the smallest particles. The transport of this peak is managed using DQMOM. The extension to HMOM was shown to yield much better agreement to MC results. However, almost perfect agreement was found for the DQMOM approach, developed by Blanquart and Pitsch [39]. This very good agreement was explained to be a consequence of the accurate prediction of the two modes, especially the mean of the second mode and the relative weight of the two modes [45]. This requirement is satisfied by enforcing a certain set of moments containing multivariate integer-order and non-integer-order moments in DQMOM. As further shown in Blanquart [75], this choice yields one quadrature node positioned at the lower size limit, and another one (in the case of 2 nodes in total) or two other nodes (in the case of 3 nodes in total) at the mean of the second mode. These findings lead to the expansion of the BiMOMIC method to HMOM introducing a quadrature node to represent the particles at the first mode.

Here, an analogy between the interpolation-based moment approaches MOMIC [86], BiMOMIC [34] and HMOM [45] and the quadrature based methods applied in this study can be identified. Representing the smallest particles properly is a well-known issue in the MOMIC-based soot models [46]. Our study reveals that the

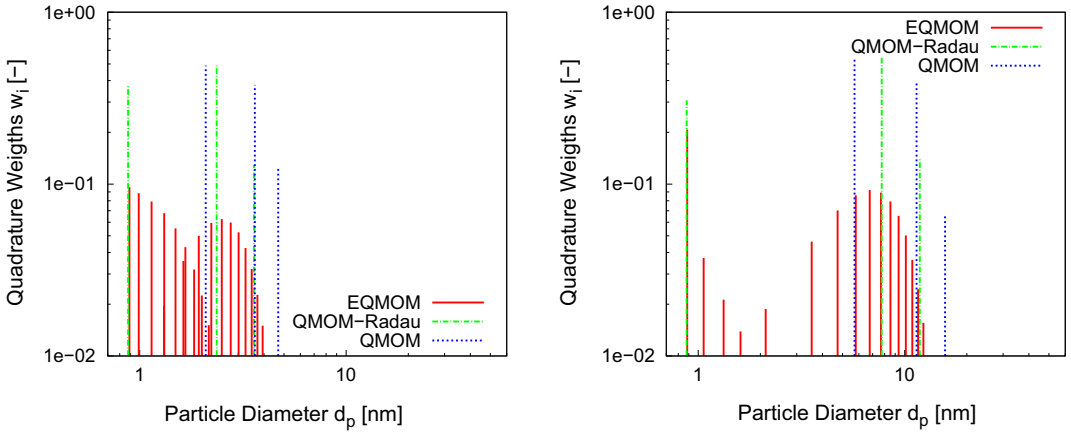

Fig. 7. Illustration of the position and the corresponding weights of the EQMOM (second Gaussian quadrature nodes), QMOM and QMOM-Radau quadrature nodes at HAB = 3.5 mm and HAB = 5.5 mm for the simulation of the $C_2H_4/O_2/Ar$ test flame with $\phi = 2.07$ [69]. For EQMOM, only the second Gaussian quadrature nodes with $w_i > 1e-2$ are shown.

same problem is present in standard QMOM. However, it is demonstrated that QMOM-Radau is a suitable extension of the moment-inversion based QMOM method to take into account the smallest soot particles in the system. Therefore, both QMOM-Radau and EQMOM are able to capture the smallest soot particles of the particle ensemble.

The above mentioned criteria, which were found to yield the high accuracy of DQMOM, also serve as an explanation for the very good precision of EQMOM. Figure 8 compares the reconstructed particle size distribution of EQMOM with MC. The reconstructed particle size distribution of EQMOM captures the behavior of the MC distribution very well in regions where the distribution is still unimodal. At higher HABs, when bimodality develops, EQMOM reveals its first differences to the MC solution in the trough region. However, EQMOM captures the shape in the coagulation-dominating regions, which are the smallest particles and the second mode and therefore satisfies the criteria to predict the mean of the second mode and the relative weight of the two modes accurately. This leads to an accuracy close to MC and DQMOM. The horizontal offset between the simulated and the measured distribution [69] is related to the choice of the pyrene dimerization nucleation model applied in this study [10].

The comparison among the univariate quadrature-based moment approaches and the MC simulation in this section reveal a high sensitivity of the coagulation term on the quadrature node position, which can lead to significant differences from a MC solution if the nodes do not represent the modes of a soot size distribution properly. More precisely, standard QMOM is not able to meet this requirement, although the evaluated nodes and weights represent the equation system (Eq. (14)) accurately. However, it is shown that the numerically robust, moment-inversion-based methods EQMOM and QMOM-Radau keep track of both particle size modes and there is no need for the numerically very challenging DQMOM approach. EQMOM, in particular, which offers detailed information on the shape of the NDF using only a few moments, is a very attractive approach.

3.3. Evaluation of the bivariate ECQMOM model

As shown in Section 3.2, EQMOM is a very good choice to close univariate moment source terms accurately. This subsection evaluates the suitability of the extension into the ECQMOM approach, which considers particle volume and surface as two independent internal coordinates to take into account particle aggregation. Therefore, ECQMOM is applied to model the soot evolution in the third test flame introduced in Section 2.4, where aggregation is known to be significant [70]. The ECQMOM results are again compared to experiments and MC simulations. Further, a pure CQMOM method is applied. However, since the previous results with the univariate models have shown that the smallest particles should be represented for all HABs, the theory of QMOM-Radau is com-bined with CQMOM in order to keep track of the first mode particles.

The major difference between the bivariate methods and the univariate approaches can be demonstrated in Fig. 9, which illustrates the distribution of the MC particles in the surface/volume (S/V) space [45]. This illustration shows, that the S/V ratio of large particles differs from the S/V ratio of a pure spherical description. Thus, the amount of aggregation can be visualized by the distance to the limit line for spheres. It is important to note that the S/V illustration and its suitability in the context of aggregation was already discussed by Mueller et al. [45] for the same flame. In this study, we use the same approach to describe the fundamental idea of CQMOM. Therefore, the bivariate moments of the MC distribution are evaluated and inverted in accordance with Section 2.1.4 to produce three volume interpolation nodes. The surface direction is described using single Dirac delta peaks, which are conditioned on the volume nodes. Figure 9 illustrates that the position of the resulting CQMOM nodes describes the S/V behavior of the MC particles. The first node is positioned at V_1 due to the application of the Gauss-Radau modification. The corresponding surface value is equal to S_1 since the smallest soot particle is assumed to be spherical.

A univariate approach which does not capture the large S/V ratio of the big aggregates underestimates the particle growth rate, which is surface-dependant. This is shown in Fig. 10a, where EQMOM and ECQMOM are compared to the experimental results of the test flame considered. Since EQMOM assumes soot particles to be spherical, it cannot describe the S/V ratio of soot aggregates and therefore underestimates the soot volume fraction in compar-ison to the experiments. This finding agrees with the results of Mueller et al. [34], where the measured soot volume fraction was compared to results of a univariate and a bivariate MOMIC approach (BiMOMIC) for the same flame. The bivariate ECQMOM approach with two Γ-distributions for V and one conditioned Dirac peak each for S, predicts the measurements more accurately.

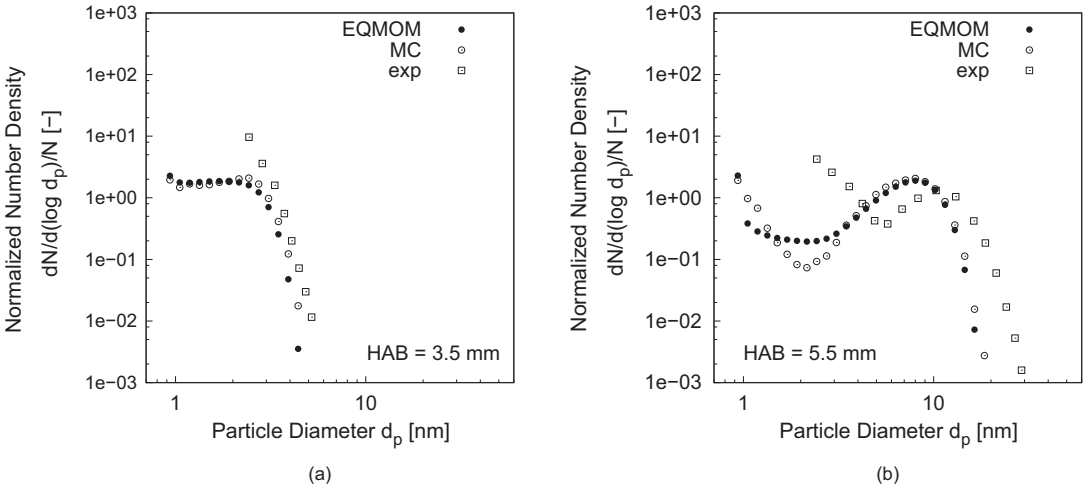

Fig. 8. Comparison of the simulated particle size distribution at HAB = 3.5 mm and HAB = 5.5 mm with the MC and EQMOM model for the burner-stabilized premixed C_2H_4/O_2/Ar test flame with $\phi = 2.07$ [69].

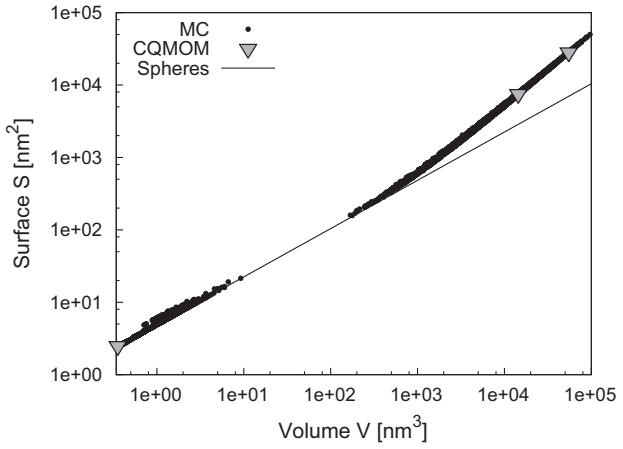

Fig. 9. Surface/Volume (S/V) illustration of the MC particle ensemble and the corresponding CQMOM quadrature nodes for the $C_2H_4/O_2/N_2$ test flame with $\phi = 2.64$ [70]. Due to aggregation, the large particles have a significantly higher S/V ratio compared to the assumption of a spherical shape.

However, considering the mean primary particle diameter d_p (Fig. 10b), the numerical predictions appear to underestimate the measured values significantly. This effect was also found in [39,75]. As Blanquart [75] pointed out, the TEM experiments mainly consider large soot particles. Therefore, only the particles of the second mode should be taken into account for comparison with the experiment. As shown in Fig. 10b, considering only parti-cles with an equivalent spherical diameter larger than $d = 5nm$ leads to significant improvement and good agreement. This par-ticular choice for the cutoff diameter is chosen as the position of the trough between the first and the second mode is located at $d \approx 5$ nm at higher HABs when bimodality is fully distinct.

The comparison of the numerical models is shown in Fig. 11. It can be seen that ECQMOM shows only minor differences to the MC simulation for the soot volume fraction and the number density. In terms of quality, CQMOM with four nodes for V and one conditioned node each for S, yields the same trends as MC and ECQMOM. However, small differences are found for both f_v and N. The same trends are observed for the mean primary particle diameter d_p and the mean primary particle number n_p. Here, ECQMOM yields some deviations to the MC solution.

It is interesting to discuss these differences referring again to the work of Mueller et al. [45], where the bivariate approaches BiMOMIC, HMOM and DQMOM were compared to MC simulations. HMOM, which captures the smallest soot particles correctly (like ECQMOM and CQMOM), revealed some differences to the MC simulations and DQMOM. Mueller et al. [45] showed that the HMOM results can be improved through minor modifications to control a different moment set, which more closely resembles the one enforced in the DQMOM model. However, it was found that this modification comes with the drawback of a significant decrease of numerical robustness and therefore, the enforcement of the default moment set of HMOM based on integer-order moments is recommended [45].

Similar to HMOM, the moment-based soot models applied in this study enforce a set of integer-order moments. Based on the rationale of these approaches, there is no free choice to control a different moment set such as the one used by Mueller et al. [45] for the DQMOM simulations. However, considering the small magnitude of the quantitative deviations to MC presented in Fig. 11 and aspects like numerical robustness, both ECQMOM and CQMOM represent very suitable approaches to model the evolu-tion of soot ensembles in the considered flames.

This assessment is supported by the fact that both ECQMOM and CQMOM are able to capture the qualitative trends of the MC simulation very well (see Fig. 11). At around HAB = 7 mm, the growth of d_p stagnates and the mean primary particle number n_p even decreases. As explained by Mueller et al. [45], the effect occurs due to the rapid coagulation of large particles in this region, which changes the ratio between small and large particles. Afterwards, as shown in Fig. 6 for the univariate methods, the coagulation process is dominated by small particles hitting large particles and therefore d_p and n_p rise again.

The evaluation of the bivariate methods reveals two major findings. First, both QMOM-based approaches, involving a combination of a suitable univariate method (EQMOM and QMOM-Radau) and a CQMOM approach to describe a bivariate NDF, show good qualitative and quantitative agreement with the experimental and the MC results. This indicates that CQMOM is able to capture the bivariate S/V characteristic of a soot particle ensemble properly. Second, ECQMOM with two Γ-distributions for the volume direction, and a single Dirac delta peak conditioned on each of these two distributions, are sufficient to close the bivariate source terms precisely. As in the univariate case, the EQMOM-based method, which offers the advantage of resolving the continuous NDF using

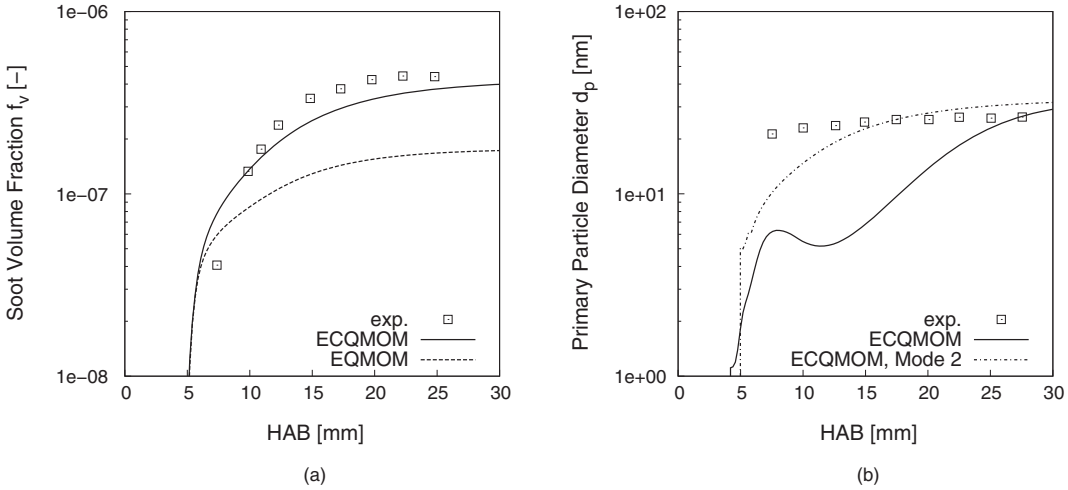

Fig. 10. Comparison of modeling results and experiments for the burner-stabilized premixed $C_2H_4/O_2/N_2$ flame with $\phi = 2.64$ [70]. (a) Comparison between the ECQMOM result for the soot volume fraction f_v with the univariate EQMOM and the experimental result. It is evident, that the univariate model underpredicts f_v significantly. (b) Comparison between the ECQMOM result for the mean primary particle diameter d_p and the experimental result. Also, the ECQMOM result for the second mode is shown in order to make the modeling results comparable to the TEM measurements conducted by Xu et al. [70].

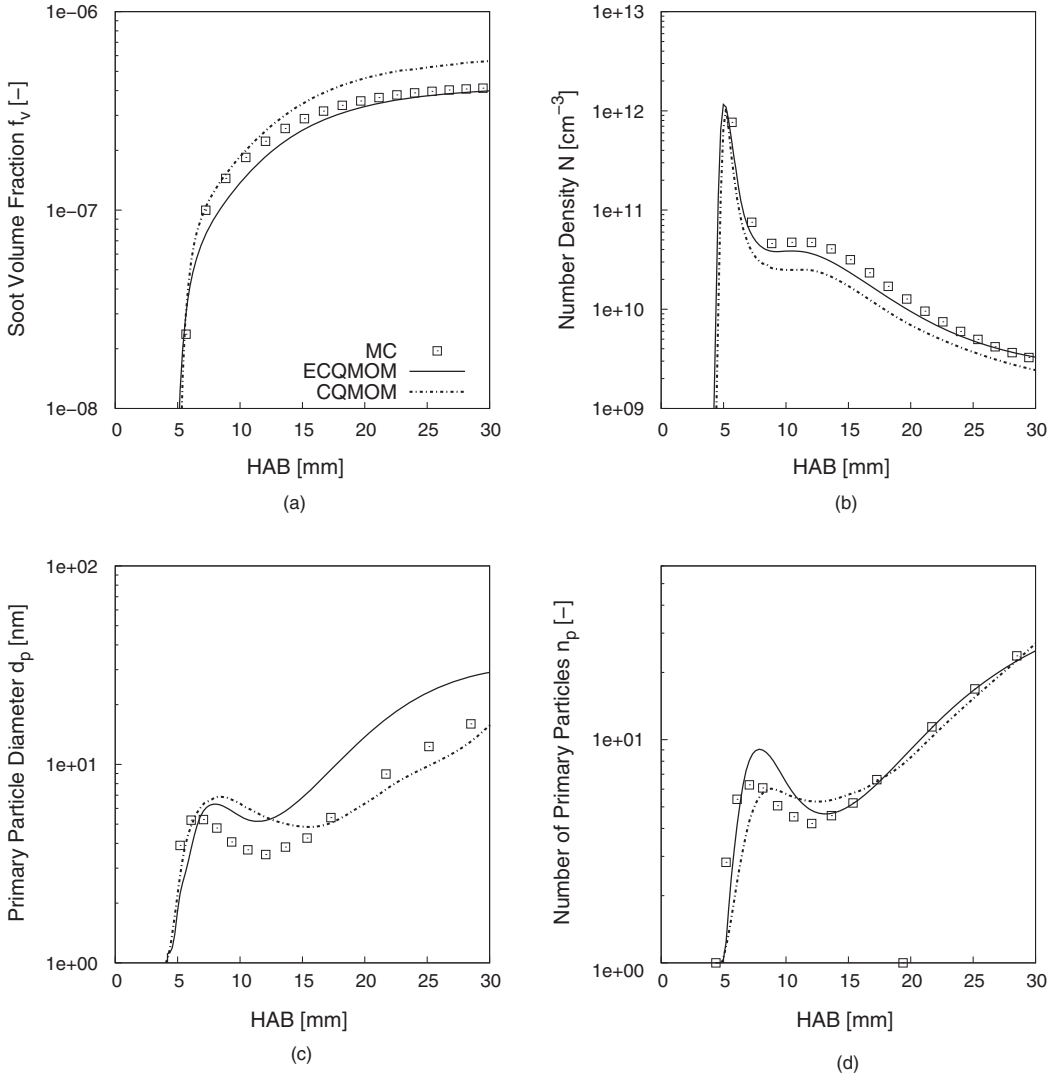

Fig. 11. Comparison between the ECQMOM, CQMOM and the MC model for the burner-stabilized premixed $C_2H_4/O_2/N_2$ flame with $\phi = 2.64$ [70]. (a) soot volume fraction f_v. (b) Number density N. (c) Mean primary particle diameter d_p. (d) Mean primary particle number n_p.

the same number of moments needed in CQMOM, is found to be very suitable both in terms of accuracy and efficiency.

4. Conclusions

In this work, the recently developed moment methods EQMOM [1] and CQMOM [2] were applied both separately and as a combined ECQMOM approach to model soot particle evolution in flames. The EQMOM-based model allows the NDF to be reconstructed, whereas CQMOM enables particle aggregation to be modeled in a numerically robust manner. The ECQMOM method combines the advantages of the two approaches.

The gas phase profiles of the investigated flames were modeled using a modified version of the well-established CRECK mechanism. The comparison between the model and experimental results revealed that the mechanism is able to predict not only the major species, but also PAHs accurately. Furthermore, it was found that the influence of CH_4 addition on the formation of soot precursors, and the laminar flame velocity of C_2H_4 mixtures at different equiva-lence ratios and pressures, are predicted well by the chemical model.

The EQMOM-based soot models were validated against experimental and other simulation results. In this process, the univariate EQMOM soot model was validated against experiments and other models based on a MC, a QMOM and a QMOM-Radau method. The validation of the univariate EQMOM method revealed two major findings. First, the availability of the NDF resolved from reconstruction offers a consistent comparison between the model and the experiments, as EQMOM allows us to omit the smallest soot particles, which are below the detection limit of a SMPS test setup, from the modeled NDF. This is a significant advantage over other moment-based methods where the shape of the NDF is unknown. Second, EQMOM was found to yield very good agreement to the MC results and is therefore very convenient to close the moment source terms of the soot model. The accuracy can be explained by the EQMOM's ability to capture both the smallest particles of the first and the large particles of the second mode properly. In particular, the permanent representation of the smallest particles was shown to be a critical requirement which cannot be met using a standard QMOM method. A QMOM-Radau method, which is a standard QMOM approach where the first interpolation node is fixed at the position of the smallest particles, yielded similar accuracy to EQMOM. However, in comparison to EQMOM, the NDF is unknown in QMOM-Radau.

In order to consider aggregation, EQMOM was extended to a bivariate ECQMOM. Again, the model was validated against experiments and other numerical models, based on MC and pure CQMOM. The basic idea of the ECQMOM model was to represent the surface of the soot particle ensemble using a Dirac delta function which is conditioned on each Γ-distribution describing the soot volume. Again, the knowledge of the continuous NDF enabled a consistent comparison between the model and experiments, as only the particles of the second mode were captured in the measurements of the primary particle diameter [70,75]. The comparison between the ECQMOM results and the MC results revealed good agreement both in terms of quality and quantity. Similar agreement was found for the pure CQMOM approach, where the same amount of moments need to be solved, but the NDF is unavailable.

In summary, the EQMOM-based models were found to be very convenient to model the soot evolution in flames.

Acknowledgments

The authors acknowledge the financial support by the Federal Ministry of Food and Agriculture in the project 'BiOtto' (Project number 22041111).

Furthermore, the authors acknowledge the financial support by the Federal Ministry of Education and Research of Germany in the framework of Virtuhcon (Project number 03Z2FN11).

Appendix A. Supplementary material

Supplementary data associated with this article can be found, in the online version.

References

[1] C. Yuan, F. Laurent, R. Fox, J. Aerosol Sci. 51 (2012) 1–23.
[2] C. Yuan, R. Fox, J. Comput. Phys. 230 (2011) 8216–8246.
[3] W. Yao, J. Zhang, A. Nadjai, T. Beji, M.A. Delichatsios, Fire Saf. J. 46 (2011) 371–387.
[4] T. Beji, J. Zhang, W. Yao, M. Delichatsios, Combust. Flame 158 (2011) 281–290.
[5] D.L. Marchisio, R.O. Fox, Computational Models for Polydisperse Particulate and Multiphase Systems, Cambridge University Press, 2013.
[6] M. Balthasar, M. Kraft, Combust. Flame 133 (2003) 289–298.
[7] M. Goodson, M. Kraft, J. Comput. Phys. 183 (2002) 210–232.
[8] R.I. Patterson, J. Singh, M. Balthasar, M. Kraft, W. Wagner, Combust. Flame 145 (2006) 638–642.
[9] J. Singh, M. Balthasar, M. Kraft, W. Wagner, Proc. Combust. Inst. 30 (2005) 1457–1465.
[10] J. Singh, R.I. Patterson, M. Kraft, H. Wang, Combust. Flame 145 (2006) 117–127.
[11] R.I.A. Patterson, J. Singh, M. Balthasar, M. Kraft, J.R. Norris, SIAM J. Sci. Comput. 28 (2006) 303–320.
[12] R.I. Patterson, M. Kraft, Combust. Flame 151 (2007) 160–172.
[13] F. Gelbart, J. Seinfeld, J. Colloid Interface Sci. 78 (1980) 485–501.
[14] R.J. Hall, M.D. Smooke, M.B. Colket, Predictions of soot dynamics in opposed jet diffusion flames, in: F. Dryer, R. Sawyer (Eds.), Physical and Chemical Aspects of Combustion: A Tribute to Irvin Glassman, vol. 4, CRC Press, 1997, pp. 189–230.
[15] M. Smooke, C. McEnally, L. Pfefferle, R. Hall, M. Colket, Combust. Flame 117 (1999) 117–139.
[16] A. D'Anna, J. Kent, Combust. Flame 144 (2006) 249–260.
[17] H. Richter, S. Granata, W.H. Green, J.B. Howard, Proc. Combust. Inst. 30 (2005) 1397–1405.
[18] K. Netzell, H. Lehtiniemi, F. Mauss, Proc. Combust. Inst. 31 (2007) 667–674.
[19] Q. Zhang, M. Thomson, H. Guo, F. Liu, G. Smallwood, Combust. Flame 156 (2009) 697–705.
[20] A. Cuoci, A. Frassoldati, T. Faravelli, E. Ranzi, Combust. Flame 156 (2009) 2010–2022.
[21] S.B. Dworkin, Q. Zhang, M.J. Thomson, N.A. Slavinskaya, U. Riedel, Combust. Flame 158 (2011) 1682–1695.
[22] T. Blacha, M.D. Domenico, P. Gerlinger, M. Aigner, Combust. Flame 159 (2012) 181–193.
[23] M. Frenklach, S.J. Harris, J. Colloid Interface Sci. 118 (1987) 252–261.
[24] M. Frenklach, H. Wang, Int. Symp. Combust. 23 (1991) 1559–1566.
[25] M. Frenklach, H. Wang, in: H. Bockhorn (Ed.), Soot Formation in Combustion, Springer-Verlag, Berlin Heidelberg New York, 1994, pp. 162–193.
[26] F. Mauss, B. Trilken, H. Breitbach, N. Peters, Soot formation in partially premixed diffusion flames at atmospheric pressure, in: H. Bockhorn (Ed.), Soot Formation in Combustion – Mechanism and Models, Springer Verlag, 1994, pp. 325–349.
[27] A. Kazakov, H. Wang, M. Frenklach, Combust. Flame 100 (1995) 111–120.
[28] A. Kazakov, M. Frenklach, Combust. Flame 114 (1998) 484–501.
[29] J. Appel, H. Bockhorn, M. Frenklach, Combust. Flame 121 (2000) 122–136.
[30] H. Pitsch, E. Riesmeier, N. Peters, Combust. Sci. Technol. 158 (2000) 389–406.
[31] M. Balthasar, F. Mauss, H. Wang, Combust. Flame 129 (2002) 204–216.
[32] C. Pels Leusden, C. Hasse, N. Peters, Proc. Combust. Inst. 29 (2002) 2383–2390.
[33] M. Balthasar, M. Frenklach, Combust. Flame 140 (2005) 130–145.
[34] M.E. Mueller, G. Blanquart, H. Pitsch, Proc. Combust. Inst. 32 (2009) 785–792.
[35] A. Zucca, D.L. Marchisio, A.A. Barresi, R.O. Fox, Chem. Eng. Sci. 61 (2006) 87–95.
[36] A. Zucca, D.L. Marchisio, M. Vanni, A.A. Barresi, AIChE J. 53 (2007) 918–931.
[37] A. Cuoci, A. Frassoldati, T. Faravelli, E. Ranzi, Kinetic modeling of soot formation in turbulent nonpremixed flames, Environ. Eng. Sci. 25 (10)(2008) 1407–1422.
[38] D.L. Marchisio, A.A. Barresi, Chem. Eng. Sci. 64 (2009) 294–303.
[39] G. Blanquart, H. Pitsch, in: H. Bockhorn, A. D'Anna, A. Sarofim, H. Wang (Eds.), Combustion Generated Fine Carbonaceous Particles, KIT Scientific Publishing, 2009.
[40] T. Chittipotula, G. Janiga, D. Thnin, Chem. Eng. Sci. 70 (2012) 67–76. 4th International Conference on Population Balance Modeling.
[41] D.L. Wright, R. McGraw, D.E. Rosner, J. Colloid Interface Sci. 236 (2001) 242–251.
[42] C. Yoon, R. McGraw, J. Aerosol Sci. 35 (2004) 561–576.
[43] C. Yoon, R. McGraw, J. Aerosol Sci. 35 (2004) 577–598.
[44] D.L. Marchisio, R.O. Fox, J. Aerosol Sci. 36 (2005) 43–73.
[45] M. Mueller, G. Blanquart, H. Pitsch, Combust. Flame 156 (2009) 1143–1155.
[46] M. Mueller, G. Blanquart, H. Pitsch, Proc. Combust. Inst. 33 (2011) 667–674.

[47] A. DAlessio, A. Barone, R. Cau, A. DAnna, P. Minutolo, Proc. Combust. Inst. 30 (2005) 2595–2603.
[48] R. Lindstedt, B. Waldheim, Proc. Combust. Inst. 34 (2013) 1861–1868.
[49] V. Vikas, C. Hauck, Z. Wang, R. Fox, J. Comput. Phys. 246 (2013) 221–241.
[50] P. Mitchell, M. Frenklach, Int. Symp. Combust. 27 (1998) 1507–1514. Twenty-Seventh Sysposium (International) on Combustion Volume One.
[51] P. Mitchell, M. Frenklach, Phys. Rev. E 67 (2003) 061407.
[52] M. Schenk, S. Lieb, H. Vieker, A. Beyer, A. Glzher, H. Wang, K. Kohse-Hinghaus, ChemPhysChem 14 (2013) 3248–3254.
[53] M. Mehta, V. Raman, R.O. Fox, Chem. Eng. Sci. 104 (2013) 1003–1018.
[54] Y. Sung, V. Raman, H. Koo, M. Mehta, R.O. Fox, AIChE J. 60 (2014) 459–472.
[55] W. Gautschi, Orthogonal Polynomials Computation and Approximation, Oxford University Press, Oxford, New York, 2004.
[56] Sweep2: Cambridge Soot Simulator, Cambridge, 2006.
[57] E. Ranzi, A. Frassoldati, R. Grana, A. Cuoci, T. Faravelli, A. Kelley, C. Law, Prog. Energy Combust. Sci. 38 (2012) 468–501.
[58] C. Saggese, A. Frassoldati, A. Cuoci, T. Faravelli, E. Ranzi, Combust. Flame 160 (2013) 1168–1190.
[59] A. Cuoci, A. Frassoldati, T. Faravelli, E. Ranzi, Combust. Flame 160 (2013) 870–886.
[60] C. Saggese, N.E. Sánchez, A. Frassoldati, A. Cuoci, T. Faravelli, M.U. Alzueta, E. Ranzi, Energy Fuels 28 (2014) 1489–1501.
[61] M.R. Djokic, K.M.V. Geem, C. Cavallotti, A. Frassoldati, E. Ranzi, G.B. Marin, Combust. Flame 161 (2014) 2739–2751.
[62] M.J. Castaldi, N.M. Marinov, C.F. Melius, J. Huang, S.M. Senkan, W.J. Pit, C.K. Westbrook, Int. Symp. Combust. 26 (1996) 693–702.
[63] J. Roesler, S. Martinot, C. McEnally, L. Pfefferle, J.-L. Delfau, C. Vovelle, Combust. Flame 134 (2003) 249–260.
[64] K. Kumar, G. Mittal, C.-J. Sung, C.K. Law, Combust. Flame 153 (2008) 343–354.
[65] M.I. Hassan, K.T. Aung, O.C. Kwon, G.M. Faeth, J. Propul. Power 14 (1998) 479–488.
[66] G. Jomaas, X. Zheng, D. Zhu, C. Law, Proc. Combust. Inst. 30 (2005) 193–200.
[67] F. Egolfopoulos, D. Zhu, C. Law, Int. Symp. Combust. 23 (1991) 471–478. Twenty-Third Symposium (International) on Combustion.
[68] T. Hirasawa, C. Sung, A. Joshi, Z. Yang, H. Wang, C. Law, Proc. Combust. Inst. 29 (2002) 1427–1434.
[69] A.D. Abid, N. Heinz, E.D. Tolmachoff, D.J. Phares, C.S. Campbell, H. Wang, Combust. Flame 154 (2008) 775–788.
[70] F. Xu, P. Sunderland, G. Faeth, Combust. Flame 108 (1997) 471–493.
[71] F. Bisetti, G. Blanquart, M.E. Mueller, H. Pitsch, Combust. Flame 159 (2012) 317–335.
[72] J. Appel, H. Bockhorn, M. Wulkow, Chemosphere 42 (2001) 635–645.
[73] K. Kuo, R. Acharya, Fundamentals of Turbulent and Multi-Phase Combustion, Wiley, 2012.
[74] G. Blanquart, H. Pitsch, Combust. Flame 156 (2009) 1614–1626.
[75] G. Blanquart, Chemical and Statistical Soot Modeling (Ph.D. thesis), Stanford University, 2008.
[76] R.G. Gordon, J. Math. Phys. 9 (1968) 655–663.
[77] J.C. Wheeler, Rocky Mt. J. Math. 4 (1974) 287–296.
[78] D. Poland, in: L. Brand, M.L. Johnson (Eds.), Numerical Computer Methods, Part D, Methods in Enzymology, vol. 383, Academic Press, 2004, pp. 427–465.
[79] A. Cuoci, A. Frassoldati, T. Faravelli, E. Ranzi, OpenSMOKE++: An object-oriented framework for the numerical modeling of reactive systems with detailed kinetic mechanisms, Comput. Phys. Commun. (2015), http://dx.doi.org/10.1016/j.cpc.2015.02.014.
[80] M. Frenklach, Phys. Chem. Chem. Phys. 4 (2002) 2028–2037.
[81] P. Desgroux, X. Mercier, K.A. Thomson, Proc. Combust. Inst. 34 (2013) 1713–1738.
[82] N.A. Eaves, A. Veshkini, C. Riese, Q. Zhang, S.B. Dworkin, M.J. Thomson, Combust. Flame 159 (2012) 3179–3190.
[83] A. Veshkini, S.B. Dworkin, M.J. Thomson, Combust. Flame 161 (2014) 3191–3200.
[84] S.E. Pratsinis, J. Colloid Interface Sci. 124 (1988) 416–427.
[85] F.E. Kruis, K.A. Kusters, S.E. Pratsinis, B. Scarlett, Aerosol Sci. Technol. 19 (1993) 514–526.
[86] M. Frenklach, Chem. Eng. Sci. 57 (2002) 2229–2239.
[87] M.E. Mueller, Large Eddy Simulation of Soot Evolution in Turbulent Reacting Flows (Ph.D. thesis), Stanford University, 2012.
[88] International sooting flame workshop, <http://www.adelaide.edu.au/cet/isfworkshop/data-sets/laminar/>, checked: 07/2014.
[89] A. Cuoci, A. Frassoldati, T. Faravelli, H. Jin, Y. Wang, K. Zhang, P. Glarborg, F. Qi, Proc. Combust. Inst. 34 (2013) 1811–1818.
[90] C. Russo, M. Alfè, J.-N. Rouzaud, F. Stanzione, A. Tregrossi, A. Ciajolo, Proc. Combust. Inst. 34 (2013) 1885–1892.
[91] B. Zhao, Z. Yang, M.V. Johnston, H. Wang, A.S. Wexler, M. Balthasar, M. Kraft, Combust. Flame 133 (2003) 173–188.